High-throughput cellular-resolution synaptic connectivity mapping *in vivo* with concurrent two-photon optogenetics and volumetric Ca^{2+} imaging

Christopher McRaven[1]*, Dimitrii Tanese[2]*, Lixia Zhang[1]*, Chao-Tsung Yang[1], Misha B. Ahrens[1], Valentina Emiliani[2], Minoru Koyama[1]§

1. Janelia Research Campus, HHMI, Ashburn VA 20147, USA
2. Institut de la Vision, Sorbonne University, Inserm S968, CNRS UMR7210, 17 Rue Moreau, 75012, Paris, France

* These authors contributed equally to this work.

§ Corresponding author

Figures: 2

Supplementary Figures: 5

Correspondence:
Minoru Koyama
Janelia Research Campus, HHMI
19700 Helix Drive,
Ashburn, VA 20147
minoru.koyama@gmail.com

Abstract

The ability to measure synaptic connectivity and properties is essential for understanding neuronal circuits. However, existing methods that allow such measurements at cellular resolution are laborious and technically demanding. Here, we describe a system that allows such measurements in a high-throughput way by combining two-photon optogenetics and volumetric Ca^{2+} imaging with whole-cell recording. We reveal a circuit motif for generating fast undulatory locomotion in zebrafish.

Main

Synapses conduct electrical signals between neurons and allow them to form circuits that ultimately control animal behavior. Thus, the ability to map synaptic connectivity and synaptic properties is essential for understanding circuit operations underlying animal behavior. Electrical signals through synapses and the dynamics of these signals can be directly measured with electrophysiological techniques such as paired whole-cell recordings. However, these techniques are hard to scale up and the yield is often low, especially *in vivo*. The development of optogenetics enabled optical control of neuronal activity has been used to assess macroscopic synaptic connectivity wherein a group of neurons is activated and their synaptic responses in other neurons are monitored via whole-cell recordings[1]. The next step is to transition from this macroscopic approach into a microscopic synaptic connectivity mapping. This requires performing high throughput optogenetic activation of presynaptic cells with single cell resolution while monitoring the photo-evoked activity of the presynaptic cell. The combination of two-photon shaped stimulation and the engineering of efficient soma-targeted opsins, called circuits optogenetics[2], opened a way to stimulate single and multiple neurons at near single-cell resolution[3–5]. Yet, the effectiveness of this approach for synaptic connectivity mapping has only been demonstrated in proof-of-principle experiments involving relatively small neuronal populations in brain slices[3,5] and has not been exploited for large-scale synaptic connectivity mapping *in vivo*. Furthermore, potential 3D off-target activations and cross talk excitation of the opsins from the imaging laser have never been rigorously assessed for such connectivity analyses.

Here we present a concurrent two-photon optogenetic stimulation and volumetric Ca^{2+} imaging system for zebrafish that allows one to induce and monitor single-cell activation in 3D and reconstruct cellular-resolution synaptic property maps in a large volume *in vivo* (Fig. 1ai), which is prohibitively difficult to accomplish with traditional techniques. We examine long-range synaptic connectivity of genetically defined spinal interneurons and reveal a circuit motif that may underlie fast undulatory movements during rapid forward locomotion. To our knowledge, this is the first demonstration of high-throughput

52 physiological measurements of synaptic properties at single-cell resolution *in vivo* that provides insights
53 into circuit operations in the nervous system.

54 For our study, we chose the high-photocurrent channelrhodopsin CoChR[6] based on previous successful
55 demonstrations of two-photon cellular stimulation with this opsin[5,7]. To monitor activated neurons by
56 Ca^{2+} imaging, we chose a genetic red Ca^{2+} indicator, jRGECO1b, which has been successfully used in
57 zebrafish[8]. This indicator allowed the imaging of Ca^{2+} response at the wavelength that minimizes the
58 imaging-induced activation of CoChR (Fig. 1a ii; Supplementary Fig. 1) and was sensitive enough to
59 detect single action potentials in zebrafish sensory neurons (Supplementary Fig. 2). For two-photon
60 activation of CoChR, we set up a two-photon patterned illumination system based on computer generated
61 holography[5] that allows the generation of photostimulation spots in arbitrary locations in 3D. We
62 achieved axial resolution of 12 μm for a 6 μm-diameter spot of illumination (Supplementary Fig. 3),
63 which is appropriate for single-cell stimulation of zebrafish neurons whose average diameter is 6.6 μm[9].
64 To perform concurrent volumetric jRGECO1b imaging, we implemented a remote-focusing system based
65 on a remote movable mirror that is translated by a voice coil motor[10]. This technique enables us to change
66 the imaging-plane without moving the objective lens, thus makes it possible to perform volumetric
67 imaging without changing the axial position of photostimulation spots (Fig. 1 aiii). This system achieves
68 axial resolution of less than 4.5 μm within the axial scanning range of 140 μm which is enough to obtain
69 two-photon imaging at cellular resolution (Supplementary Fig. 4).

70 To reach cellular resolution for opsin stimulation, we fused CoChR with the soma-localization sequence
71 from the mammalian potassium channel Kv2.1[3] to target its expression to cell bodies. We then generated
72 two UAS transgenic lines: one that expresses CoChR fused with the Kv2.1 sequence (hereafter referred as
73 CoChR-EGFP-Kv2.1), and one that expresses jRGECO1b (Fig. 1b) to take advantage of stronger but
74 sparser expression one can attain with the Gal4/UAS system. Using these optical setups and transgenic
75 lines, we examined the amount of imaging-induced activation of CoChR in a practical experimental
76 condition in hindbrain neurons (Fig. 1c). To monitor subthreshold activation of CoChR during the

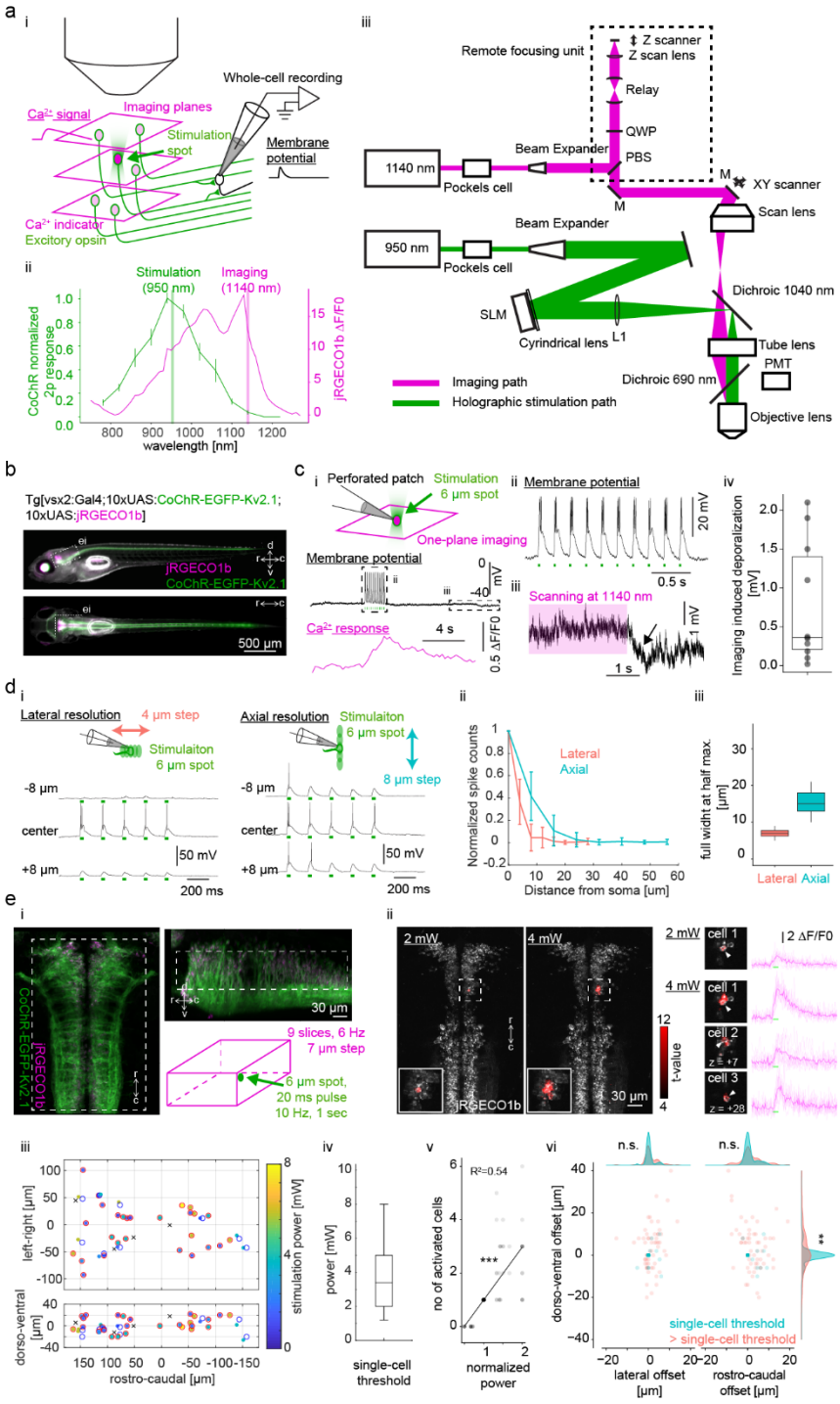

Figure 1. Concurrent two-photon optogenetics and volumetric Ca^{2+} imaging for high-throughput synaptic connectivity mapping.

a. (i) A schematic of the high-throughput cellular synaptic connectivity mapping using two-photon optogenetics and volumetric imaging. A genetically defined cell group is co-labeled with Ca^{2+} indicator (magenta) and excitatory opsin (green). Multiplane imaging is used to monitor the 3D distribution of the photo-evoked activation. Postsynatpic potential is monitored in a cell of interest by whole-cell recording. (ii) Normalized response of two-photon-induced activation of CoChR (left y-axis, green) and ΔF/F0 of jRGECO1b (right y-axis, magenta) as a function of wavelength. Excitation wavelength for photostimulation (950 nm) was chosen based on the normalized curve. To minimize imaging-induced activation of opsin-expressing neurons and reach high Ca^{2+} sensitivity, imaging was done at 1140 nm. (iii) Optical setup for simultaneous volumetric imaging and single-cell stimulation. The stimulation path is shown in green. The imaging path is shown in magenta. The remote focusing unit is highlighted with a dotted rectangle. PBS, polarizing beam splitter; QWP, quarter wave plate; SLM, spatial light modulator; PMT, photomultiplier tube; M, mirror. **b.** A transgenic zebrafish expressing CoChR-EGFP-Kv2.1 (green) and jRGECO1b (magenta) in V2a neurons in the side view (top) and the dorsal view (bottom). d, dorsal; v, ventral; r, rostral; c, caudal. The dotted whited rectangle indicates the region show in the panel ei. **c.** (i) Experimental setup for assessing imaging-induced activation of opsin-expressing cells. Hindbrain V2a were co-labeled with CoChR-EGFP-Kv2.1 and jRGECO1b and their membrane potentials were monitored by perforated patch recordings. The patched cell was stimulated by two-photon holographic illumination. Ca^{2+} response was monitored by jRGECO1b imaging. An example trace of membrane potential (top, black trace), stimulation pulses (green dots, 2 mW, 20 ms, 5 Hz), and Ca^{2+} response (bottom, magenta). (ii) A close up view of the action potentials induced by stimulation pulses. (iii) Imaging-induced depolarization. The duration of the imaging is shown with the magenta rectangle. An arrow highlights the repolarization after the end of the imaging scan. (iv) Imaging-induced depolarization in the neurons that elicited action potentials in response to stimulation (n = 10 cells). **d.** Physiological measurement of spatial resolution of holographic stimulation in neurons expressing CoChR-EGFP-Kv2.1. (i) Whole-cell recordings were performed in hindbrain V2a neurons expressing CoChR-Kv2.1. Lateral resolution was examined by scanning the 6 µm diameter stimulation spot laterally by moving the sample in 4 µm step (left). A train of stimulation pulses (20 ms, 5 Hz) were delivered to induce spiking activity. The stimulation power was chosen to elicit reliable spiking across trials (4 mW). Axial resolution was similarly examined by moving the objective lens axially in 8 µm step (right). (ii) Normalized stimulation-induced spike counts as a function of distance

from soma in lateral direction (orange, n = 14 cells) and in axial direction (cyan, n = 13 cells). (iii) Distribution of lateral and axial resolution (lateral, n = 14 cells; axial, n = 13 cells). Spatial resolution is defined as the full width at half maximum of the stimulation induced spike counts. **e.** Assessment of single-cell stimulation with volumetric jRGECO1b imaging. (i) The region of the hindbrain used for this experiment is indicated by a dotted white rectangle in the dorsal view (left) and the side view (top right). CoChR-EGFP-Kv2.1, green; jRGECO1b, magenta. Nine optical planes were acquired at 7-µm step at 6 Hz (bottom right, magenta cube). A 6-µm spot two-photon illumination was delivered in a 1-sec train of 20 ms pulses at 10 Hz (green). (ii) Examples of stimulations at the power just enough to activate the target cell (2 mW) and at the power that led to the activation of off-target cells (4 mW). Activated cells detected by regression analysis (see Methods) are shown in red based on their t-values on top of the dorsal view of the jRGECO1b volume. The activated cells and their jRGECO1b timecourses were shown on the right (thick magenta line, average response; thin magenta lines, individual responses). Z value indicates the offset in the axial direction in µm from the target cell. (iii) Spatial distribution of the targeted hindbrain V2a neurons (40 targets from 4 fish) and the activated cells at the condition that led to single-cell activation (36 targets). Red open circles indicate the targets with successful single-cell on-target activation (27 targets). Blue open circles indicate the targets with successful single-cell but off-target activation (9 targets). Black crosses indicate the targets with no successful single-cell activation (4 targets). The activated cells for successful single-cell activation are indicated by filled circles with their color coding the stimulation power. (iv) Stimulation power used for single-cell stimulation (n = 36 targets). (v) Number of activated cells as a function of the normalized power (normalized to the power used for single-cell stimulation for each target) (n = 36 targets). The data was fitted with a linear regression (black line). The regression coefficient was statistically significant (P = 2.6e-17). (vi) The location of activated cells relative to the target cell at the power for single-cell stimulation (cyan) and at the power just above the power for single-cell stimulation (orange) (n = 36 targets). The distribution changed significantly in the dorso-ventral axis (Kolmogorov-Smirnov test, P = 9.6e-3).

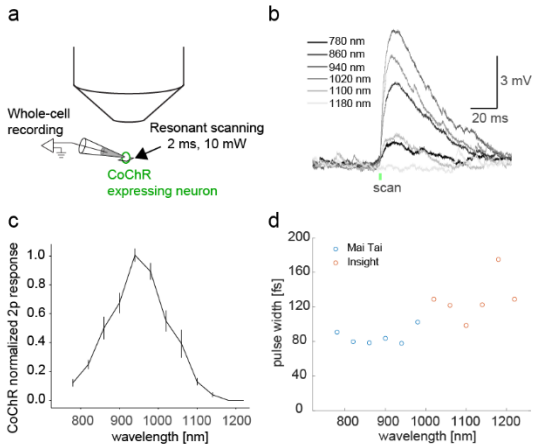

Supplementary Figure 1. Wavelength-dependent two-photon activation of CoChR-expressing neurons
a. Experimental setup. Subthreshold response in a hindbrain V2a neuron expressing CoChR was monitored by whole-cell recording. The recorded cell was stimulated by resonant raster scanning of femtosecond laser over the cell body (2 ms, 10 mW). **b.** Example traces of subthreshold response from 780 nm to 1180 nm. The timing of the stimulation scanning is indicated by a green dot. **c.** Normalized response amplitude as a function of wavelength (n = 10 cells). **d.** Pulse widths of femtosecond laser as a function of wavelength. Measurement from two different laser sources are combined (blue, Mai Tai; red, Insight).

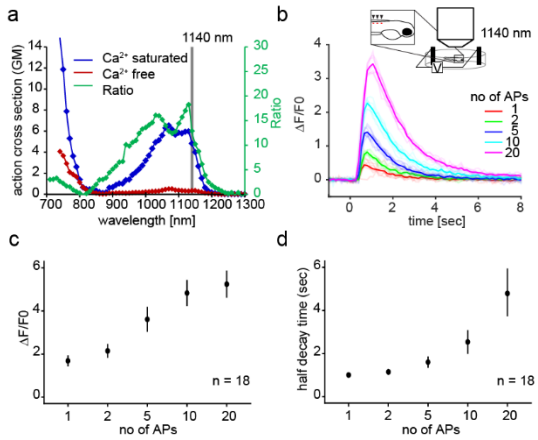

Supplementary Figure 2. Sensitivity of jRGECO1b in zebrafish spinal sensory neurons
a. Two-photon action cross section of jRGECO1b in Ca^{2+}-free (blue line) and Ca^{2+}-saturated (red line) states. Green line shows the ratio between the two states. **b.** Two-photon imaging of zebrafish Rohon-Beard cells expressing jRGECO1b at 1140 nm. Example traces of jRGECO1b Ca^{2+} response to action potentials elicited by electrical shocks (50 Hz). **c.** Fluorescence fold change of jRGECO1b as a function of number of action potentials (APs). **d.** Half decay time of jRGECO1b as a function of number of action potentials (APs).

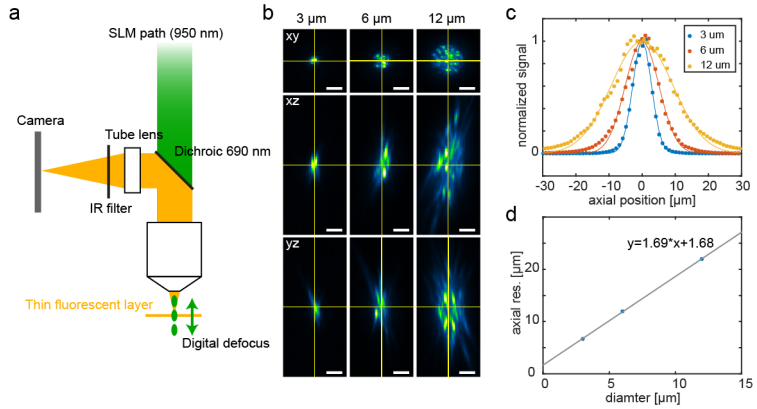

Supplementary Figure 3. Axial profile of two-photon holographic stimulation
a. Experimental setup for characterizing axial resolution of two-photon holographic beam. A cover glass with a thin layer of fluorescent dye is brought to the focal plane of the objective lens. A holographic spot of a given diameter is digitally focused at different depths while imaging the resulting fluorescence at the focal plane of the objective lens with a camera. **b.** Cross sections of holographic spots with variable diameters (3, 6 and 12 µm). **c.** Axial profiles of the variably sized holographic spots (3, 6 and 12 µm). Normalized integrated fluorescent signal is plotted as a function of axial position. **d.** Axial resolution as a function of spot diameter, showing a linear relationship between them.

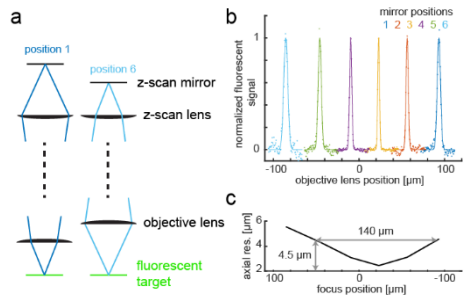

Supplementary Figure 4. Axial resolution of the remote focusing system
a. Experimental procedure. Z-scan mirror was positioned by a voice coil to change the focus of the scanning beam (dark blue, position 1; cyan, position6). For each mirror position, we scan the objective lens axially and monitor the fluorescent signal from the fluorescent target (green) to characterize the axial extent of the point spread function (PSF). **b.** Normalized fluorescent signal as a function of objective lens position. Signal profiles were plotted separately for each mirror position (1 to 6). Zero in the x-axis ("objective lens position") is defined as the position where the fluorescent target is in focus when the remote focusing unit is bypassed. **c.** Axial extent of the PSF as a function of the focus position. Axial extent is defined as full width at half maximum of the normalized fluorescent signal. Note that axial resolution stays below 4.5 µm for 140-µm axial scanning range.

imaging of jRGECO1b expressed in cytosol, we used perforated patch recording so as to retain jRGECO1b in the cytosol while recording. For this analysis, we only included neurons with high CoChR expression that exhibited reliable action potentials in response to stimulation pulses (Fig. 1c i,ii) and used single-plane imaging with high enough imaging power (6.5 mW) to reliably detect the fluorescent increase of jRGECO1b (Fig. 1ci). As a given neuron is scanned more frequently with single-plane imaging, this test provides an upper estimate of the imaging artifact. We measured the hyperpolarization after the end of imaging to examine the imaging-induced activation at a steady state (Fig. 1ciii). The activation ranged from 0 to 2.1 mV with median of 0.4 mV (Fig. 1civ), showing that our optical

85 configuration minimizes the chance of causing spurious off-target activations during single-cell
86 stimulation or state changes of the imaged area.

87 Next, we examined the spatial resolution of our two-photon photoactivation system using two approaches.
88 First, we used whole-cell recording to examine how spiking response to a 6-μm stimulation spot changes
89 as a function of the offset between the stimulation spot and the target (Fig. 1d). The spatial resolution of
90 stimulation based on spiking response was 6 μm in the lateral direction and 15 μm in the axial direction
91 (n=12), which is on par with that of the optical confinement of the two-photon holographic illumination
92 (Supplementary Fig. 3). We then examined if it was possible to achieve single-cell stimulation of
93 hindbrain neurons using concurrent volumetric jRGECO1b imaging (Fig. 1e). We used a slice interval of
94 7 μm which is on par with the average soma size of neurons in larval zebrafish neurons[9] so that we do not
95 miss collateral activation of nearby neurons (Fig. 1e i). By detecting activated cells based on online
96 regression analysis (see Methods), we tuned the stimulation power so that we stimulate only a single cell
97 (Fig. 1e ii). Out of 40 targets we examined throughout the hindbrain population (Fig. 1e iii), we were able
98 to find the power that activates just one cell in 36 cases, 9 of which activated an off-target cell presumably
99 due to imperfect soma localization of CoChR by the Kv2.1 sequence[5] and higher excitability and CoChR
100 expression of the off-target cell. The power required for single-cell stimulation varied from 1.2 mW to 8
101 mW with median of 3.4 mW (Fig. 1e iv). The number of activated cells increased significantly when the
102 power was set above the minimal power for single-cell stimulation (Fig. 1e v), further suggesting the
103 importance of using the minimum power for each target for precise singe-cell and multi-cell activations.
104 Specifically, collateral activations observed at suprathreshold conditions showed substantial spread in the
105 axial direction (Fig. 1e vi; Kolmogorov-Smirnov test, $P = 0.0096$). This is probably due to the fact that
106 higher excitation powers, approaching the saturation of the opsin response, axially enlarge the effective
107 volume of the optical stimulation, as previously discussed[5]. This further suggests the importance of
108 concurrent volumetric imaging with cellular z resolution to assess collateral activation (Fig. 1e i). Taken
109 together, we showed that it is possible to attain single-cell stimulation when the stimulation power was

110 carefully tuned using the combination of two-photon opsin stimulation, sparse opsin expression, and
111 crosstalk-free volumetric functional imaging.

112 To demonstrate the utility of this system for mapping synaptic connectivity, we focused on the
113 investigation of the connectivity from spinal V2a neurons to axial primary motoneurons (PMNs). Spinal
114 V2a neurons are glutamatergic ipsilateral projecting neurons that play a critical role in locomotion[11].
115 Their connectivity to motoneurons has been examined with both paired whole-cell recordings and
116 electron microscopy[12–14]. However, these analyses have been restricted to local connections within a few
117 spinal segments. To examine their long-range connectivity, we patched PMNs in spinal segment 23 and
118 stimulated single V2a neurons expressing CoChR-Kv2.1 and jRGECO1b from segment 6 to segment 21
119 (Fig. 2a i, n = 6 fish). In 85% of the stimulation sites, we were able to achieve single-cell activation
120 (358/419; Fig. 2a ii). Twenty seven percent of the cells we activated elicited membrane depolarization in
121 the recorded PMNs in synchrony with the stimulation pulses (98/358; Fig. 2b i, ii). We found two distinct
122 response types based on the kinetics of membrane depolarization that are not mutually exclusive. The first
123 type had a fast rise time constant and was observed in response to 12% of the stimulated cells (Fig. 2b i;
124 half rise time = 0.57 ± 0.35 ms, n = 43). This time constant is compatible with those of postsynaptic
125 potentials[14], indicating they are synaptically connected to the recorded PMNs. The second type had a
126 slower rise time constant and was observed in response to 21% of the stimulated cells (Fig. 2b ii; half rise
127 time = 15.3 ± 5.4 ms, n = 74). As motoneurons do not express CoChR in this preparation, the second
128 type is likely to be indirect excitation through electrical coupling among axial motoneurons[14–16].
129 Coexistence of both response types were observed in 18% of the responding cell (18/98). The probability
130 of finding synaptically connected cells was significantly biased towards the dorsal spinal cord (Fig. 2c; P
131 = 6.5e-6). The bias in the rostrocaudal direction was also significant but less prominent with some
132 connected cells up to 15 segments rostral to the PMN (Fig. 2c; P = 0.015). This not only confirms
133 previous observations about the selective innervation of dorsal V2a neurons to PMNs[12,13] but also extends
134 this connectivity pattern to long-range connections. The probability of finding coupled cells was

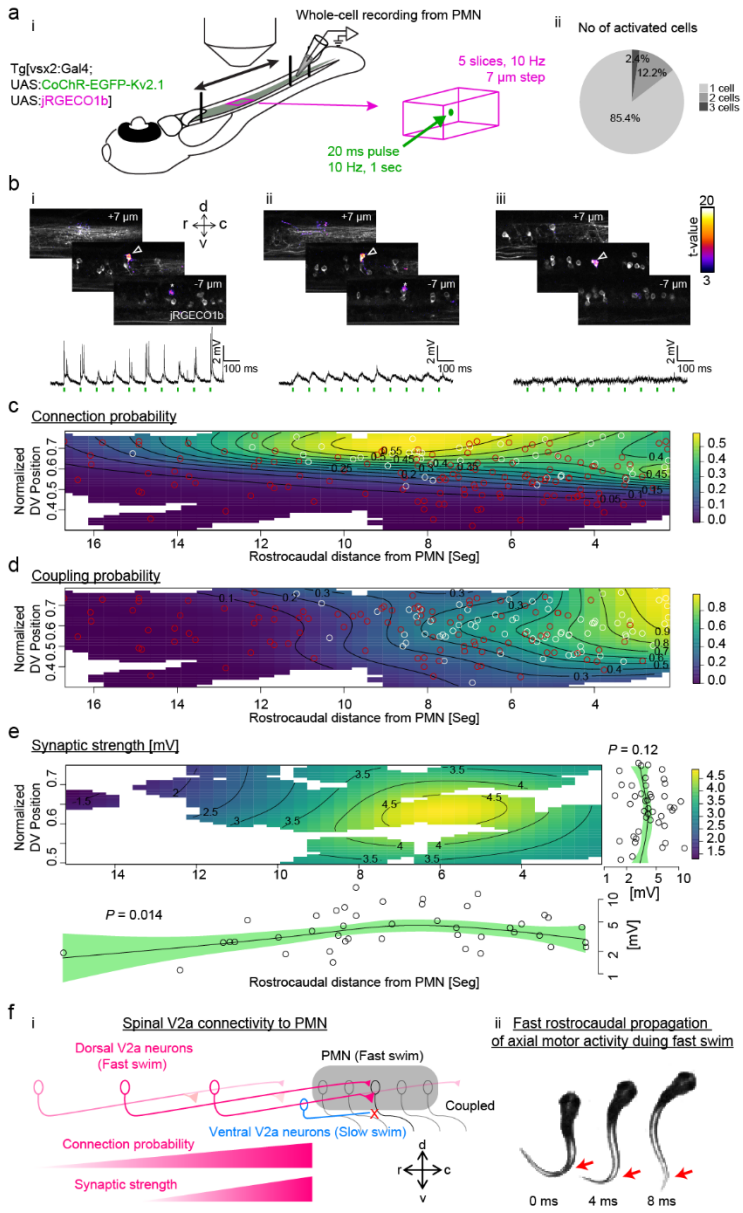

Figure 2. Large-scale synaptic connectivity mapping from spinal V2a neurons to primary motoneurons assisted by two-photon optogenetics and imaging

a. (i) Experimental procedure. Whole-cell recording was established in a primary motoneuron (PMN) in the caudal spinal cord (spinal segment 23) in the transgenic line expressing CoChR-EGFP-Kv2.1 and jRGECO1b in V2a neurons (indicated by the shaded area). Spinal V2a neurons rostral to the patched PMN were activated one-by-one by holographic two-photon stimulation. Simultaneous volumetric imaging of jRGECO1b was performed to examine the resulting activation. To cover V2a neurons up to 17 segments rostral to the patched PMN, the sample was scanned along the rostrocaudal direction. (ii) Number of activated V2a neurons per photostimulation sites (n = 419 sites, N = 6 fish) **b.** Examples of successful single-cell stimulation of spinal V2a neurons. (i) An example of V2a neuron activation that led to fast membrane depolarizations in a PMN. Three sagittal slices showing the activated cells (open arrowhead) and nearby neurons and neuropil. The activated pixels were detected by regression analysis and color-coded by their t-values. The target cell is indicated by an open arrow. The asterisk at the plane -7 µm indicates the part of the target cell. d, dorsal; v, ventral; r, rostral; c, caudal. The membrane potential from the patched PMN during the stimulation is plotted at the bottom. The individual stimulation pulses are indicated by green bars. Note the fast depolarizations triggered by stimulation pulses, indicating the stimulated V2a neuron is synaptically connected to the PMN. (ii) An example of V2a neuron activation that led to slow membrane depolarization in the PMN. This panel is similarly organized to i. Note that the stimulation pulses triggered slow depolarizations distinct from synaptic potential. (iii) An example of V2a neuron activation that led to no discernible responses in the PMN. No consistent postsynaptic potentials were observed in sync with the stimulation pulses. **c.** Spatial probability map of V2a neurons synaptically connected to PMN. The positions of the singly stimulated V2a neurons are plotted. The x-axis indicates the distance from the patched PMN in the caudal spinal cord in the unit of segments and the y-axis indicates the dorsoventral position normalized to the full thickness of the cord at a given segment (see Methods). Synaptically connected cells are indicated by white circles and non-connected ones are indicated by red circles. The probability density was estimated by generalized additive model (see Methods) and color coded. Both dorsoventral and rostrocaudal positions showed significant effect to the connection probability (dorsoventral position, P = 6.5e-6; rostrocaudal position, P = 0.015). **d.** Spatial probability map of V2a neurons exhibiting putative indirect electrical coupling (slow depolarization) to PMN. This panel is similarly organized to c. White circles, coupled cells; red circles, non-coupled cells. The rostral caudal position showed significant effect (P = 7.5e-9). **e.** Spatial distribution of the synaptic strength from the synaptically connected V2a neurons to PMN. This panel is similarly organized to c and d except that the partial effect of the dorsoventral position is plotted on the right and that of the rostrocaudal position is plotted on the bottom. Note the significant effect of rostrocaudal position. **f.** A proposed circuit motif of dorsal spinal V2a neurons involved in fast locomotion that entails fast rostrocaudal propagation of axial muscle activity. (i) PMNs are only recruited during fast swim and electrically coupled across local spinal segments (gray shade). PMNs do not receive inputs from ventral V2a neurons that are recruited during slow swim (blue) but do receive long-range inputs from dorsal V2a neurons that are recruited during fast swim (magenta). Both the connection probability and the synaptic strength decline as the distance between the dorsal V2a neurons and PMNs increases. This creates a long-range gradient of excitatory drive in the rostrocaudal direction, which is suitable for generating fast rostrocadual propagation of axial muscle activity. (ii) Fast rostrocaudal propagation of axial muscle activity during fast swim. Consecutive images of fish during fast swim are shown with the time interval of 4 ms. The regions of the tail where the curvature changes its sign are indicated with red arrows in all images to highlight the rostrocaudal propagation of axial motor activity during fast swim.

135 significantly biased to the nearby segments with more than half of the cells within 6 segments from the
136 recorded PMNs (Fig. 2d; $P = 7.5e-9$) in agreement with a previous report[14]. The distribution of synaptic
137 strength also showed significant bias in the rostrocaudal direction with stronger connections from the
138 closer V2a neurons (Fig. 2e; $P = 0.014$). Such a rostrocaudal gradient of excitatory drive has been
139 suggested to play an important role in the rostrocaudal propagation of axial muscle activity[17,18] and was
140 also hypothesized to arise from either more abundant excitatory neurons in the rostral spinal cord[18,19] or
141 their more prominent descending projections[17,20]. Here we provide experimental evidence for long-range
142 rostrocaudal gradients of synaptic strength and connection probability from a class of excitatory
143 interneurons that is selectively recruited during fast locomotion[21,12] (Fig. 2f i). This evidence suggests the
144 role of this circuit motif in fast undulatory movements during rapid forward locomotion. (Fig. 2f ii).

145 In summary, we established a system that enables the efficient discovery of cellular-level circuit motifs *in*
146 *vivo.* The combination of circuit optogenetics and concurrent volumetric Ca^{2+} imaging assures single-cell
147 precision optical activation of putative presynaptic neurons. High temporal resolution of electrical
148 recording of postsynaptic response enables the identification of different types of postsynaptic response
149 based on its kinetics. Thus, this system allows single-cell precision optical mapping of presynaptic
150 neurons and detailed characterization of synaptic dynamics on a large scale and enables efficient
151 discovery of circuit motifs as we demonstrated here. Temporally precise multi-spot photoactivation also
152 enables the investigation of synaptic summation. This approach, combined with rapidly improving
153 sensitive and fast voltage indicators, can pave the way for an all-optical synaptic mapping to assess
154 longitudinal changes in synaptic properties across many temporal scales in a living animal.

155 # Methods

156 ## Fish care

157 Zebrafish larvae were obtained from an in-house breeding colony of adults maintained at 28.5°C on a 14-
158 10 hr light-dark cycle. Embryos were raised in a separate incubator but at the same temperature and on
159 the same light-dark cycle. Larvae at 3 and 5 days post-fertilization (dpf) were used for this study. All
160 experiments presented in this study were conducted in accordance with the animal research guidelines
161 from the National Institutes of Health and were approved by the Institutional Animal Care and Use
162 Committee and Institutional Biosafety Committee of Janelia Research Campus (16-145).

163 ## Transgenic fish

164 The following previously published transgenic lines were used in this study: TgBAC(vsx2:Gal4)[22];
165 Tg(10xUAS:CoChR-EGFP)*if44* [8]; Tg(elavl3:Gal4)[23]. Tg(10xUAS:CoChR-EGFP-Kv2.1) and
166 Tg(10xUAS:jRGECO1b) were generated with the Tol2 system (Urasaki, Morvan, and Kawakami 2006)
167 using the corresponding plasmids prepared from the following reagents.

168 1. Tol2kit[24]
169 2. FCK-gene86-GFP (CoChR)[6]
170 3. pTol2-elavl3-Voltron-ST(Kv2.1)[25]
171 4. pTol2-elavl3-jRGECO1b[8]

172 ## Optics

173 Two-photon computer generated holography and remote-focusing systems were built on top of a custom
174 microscope equipped with a two-photon resonant scanning system and a one-photon widefield
175 epifluorescence system as described previously[25,26]. Briefly, a resonant scanner (Thorlabs, MPM-2PKIT)
176 was used to scan the femtosecond laser (MKS Instruments, Mai Tai HP Deep See and Insight Deep See,

177 MA) through a scan lens assembly consisting of three achromatic lenses (Thorlabs, AC254-150-C,
178 AC508-200-B and AC508-200-B), a tube lens (Nikon, MXA22018) and a 25x objective lens (Leica,
179 HCX IRAPO L 25x/0.95 W, Germany). Excited fluorescence by two-photon scanning was directed to
180 GaAsP photomultiplier tubes (Hamamatsu, H10770-40 SEL) by a dichroic mirror (Semrock, FF735-
181 Di02) and spectrally separated to three channels by dichroic mirrors (Semrock, FF562-Di03 and FF650-
182 Di01) and emission filters (Semrock, FF01-520/70-30-D, FF01-625/90, and FF01-731/137). Two-photon
183 images were collected using ScanImage (Vidrio Technologies, VA). Epi-fluorescence for widefield
184 imaging was directed to the path by an image-splitting dichroic mirror (Semrock, F640-FDi02-t3) and
185 filtered by an IR filter (Semrock, FF01-750sp) and an appropriate emission filter, and then images were
186 formed on the camera (PCO, pco.edge 4.2, Germany) through a tube lens (Nikon, MXA22018). Images
187 were collected using µManager (https://micro-manager.org/). The initial dichroic mirror for each path is
188 on a miniature stage to switch between the two detection pathways.

189 Computer generated holography system

190 Two-photon illumination patterns were obtained with computer-generated holography, a technique based
191 on the phase modulation of the laser wavefront by the use of a spatial light modulator (SLM) [5]. The beam
192 from a femtosecond laser (MKS instruments, Mai Tai HP, Deep See, MA) was enlarged by a telescope
193 and reflected off the SLM (Hamamatsu, LCOS-SLM X10468-07) and then projected on the back focal
194 plane of the objective lens with a double afocal telescope (f = 30 mm, Thorlabs AC254-030-B;
195 f = 100 mm, Thorlabs AC508-100-B; f = 200 mm, Thorlabs AC508-200-B; f = 300 mm, Thorlabs AC508-
196 300-B). The zeroth order of diffraction was eliminated by introducing a single cylindrical lens (Thorlabs,
197 LJ1516L1)[27]. The photoactivation beam were directed to the objective lens through a dichroic mirror
198 (Semrock, Di02-R1064). A phase profile for a given illumination pattern was calculated using the
199 Gerchberg and Saxton (GS) iterative algorithm[28,29], implemented on a custom-designed software (Wave
200 Front Designer). Lens-phase modulations were added to 2D-phase holograms to enable remote axial
201 displacement and 3D positioning of 2D light patterns. The performance of the illumination system for

202 single cell photostimulation was assessed by the reconstruction of the illumination volumes
203 corresponding to circular holographic patterns (diameter: 3 μm, 6 μm and 12 μm) (Supplementary Fig. 3).
204 A thin layer of rhodamine-6G (spin coated and dried on a glass coverslip) was positioned at the focal
205 plane of the objective lens and then a disk illumination pattern was scanned axially by the lens-phase
206 modulation and the resulting fluorescence was imaged by the widefield epifluorescence imaging setup
207 described above (Supplementary Fig. 3a). The fluorescence signal was integrated over the spot surface
208 and plotted as a function of the axial position specified by the lens-phase modulation (Supplementary Fig.
209 3c). The effective axial shift induced by the nominal digital phase-modulation was verified in a dual
210 microscope configuration by a mechanical axial scan of the objective lens, as previously described[27,5].

211 The holographic illumination system was calibrated before each experiment by verifying the spatial
212 alignment between the patterns of illumination and the imaging system. We generated a bi-dimensional
213 multi-spot holographic pattern (typically 5 diffraction limited spots) and we used it to bleach a thick
214 fluorescence plate (Chroma, part No. 92001). The pattern was axially shifted by a lens-phase modulation
215 in order to bleach the fluorescent plate at different depths (typically five planes over ~200 μm along the z
216 axis). Then we re-imaged the bleached pattern with the two-photon scanning imaging system to obtain the
217 exact positioning of the holographic spots in the coordinates of the imaging system. An affine
218 transformation (x-y-z stretch, translation and rotation) between the nominal and the measured position of
219 the spots was identified for each plane. The parameters of such transformation were linearly interpolated
220 to obtain the required transformation matrix at any depth.

221 After such calibrations, we examined the targeting accuracy by bleaching the fluorescent plate with an
222 arbitrary multi-point 3D illumination patterns (Supplementary Fig. 5), ensuring micrometric precision in
223 the control of the spot locations.

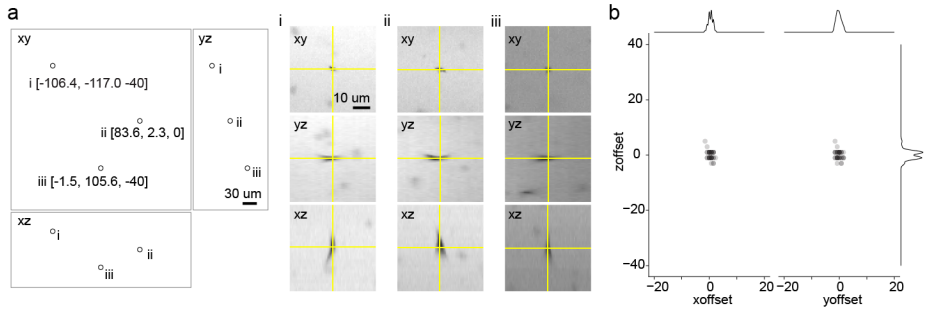

Supplementary Figure 5. Accuracy of 3D targeting *in vitro* tested by bleaching fluorescent plate

a. Examples of bleached spots. (left) Location of three bleached spots in xy, yz, and xz views. (right) Close-up views of bleached spots. **b.** The location of bleached spots relative to the target location (n = 42 targets).

Remote-focusing system

An axial scanning system for two-photon imaging was implemented based on a remote movable mirror that is conjugate to the specimen plane and translated by a voice coil motor similar to the system described previously[10] (Figure 1a iii). This system is built on top of the existing two-photon imaging system in a way that can be engaged on demand using the polarizing beam splitters (Thorlabs, PBS203) mounted on a sliding stage. When the beam is directed to the system, it goes through a telescope (f1 = 75 mm Thorlabs AC254-075-C, f2 = 125 mm Thorlabs AC254-125-C) and an axial scan lens assembly consisting of three achromats lenses (Thorlabs AC254-100-C, AC254-75-C and AC254-100-C) before being reflected by the axial scan mirror (Thorlabs, PF03-03-P01) mounted on a voice coil (equipment solutions, LFA-2004). A quarter-wave plate (Thorlabs, AQWP05M-980) was inserted in the path close to the polarizing beam splitter so that the beam reflected by the mirror goes past the polarizing beam splitter and to the xy-scanning module. Basic optical performance was assessed by measuring the point spread function (Supplementary Fig. 4). We chose 6 mirror positions and in each position we took a z-stack of a two-photon excitable target by moving the objective lens by a piezo objective scanner (PI, P-725K129, Germany) with a 0.5 μm step size (Supplementary Fig. 4a). The signal profile was plotted as a function of the position of the objective lens for each mirror position (Supplementary Fig. 4b). Then the full width at

241 half maximum for each mirror position was plotted as a function of the focus position (Supplementary
242 Fig. 4c).

243 Assessment of the imaging-induced artifact by simultaneous perforated patch 244 recording and Ca^{2+} imaging from holographically stimulated neurons

245 Perforated patch recordings were made in hindbrain neurons expressing CoChR-EGFP-Kv2.1 and
246 jRGECO1b in Tg[vsx2:Gal4;10xUAS:CoChR-EGFP-Kv2.1;10xUAS:jRGECO1b] using the procedure
247 described previously with some modifications[26]. Briefly, 5 dpf fish were paralyzed by 1 mg/ml alpha-
248 bungarotoxin (MilliporeSigma, 203980, MO) dissolved in system water and then anesthetized with MS-
249 222 and secured with etched tungsten pins through the notochord to a glass-bottom dish coated with
250 Sylgard (Dow Corning, Sylgard 184, MA). Then the solution was exchanged with extracellular solution
251 containing MS-222 (134 mM NaCl, 2.9 mM KCl, 1.2 mM MgCl2, 2.1 mM CaCl2, 10 mM HEPES, 10
252 mM glucose, 0.3 mM MS-222, adjusted to pH 7.8 with NaOH). Then the ventral surface of the hindbrain
253 was carefully exposed using a tungsten pin and fine forceps and the solution was exchanged to
254 extracellular solution without MS-222. Ventral neurons in the middle hindbrain (hindbrain segment 3, 4
255 and 5) were targeted based on fluorescence and scanned Dodt gradient contrast image acquired with the
256 custom two-photon microscope. Nystatin-based perforated whole-cell recordings were established using
257 the procedure described previously. Briefly, nystatin-containing intracellular solution was freshly
258 prepared from 50 µL intracellular solution (125 mM K-gluconate, 2.5 mM MgCl2, 10 mM EGTA, 10
259 mM HEPES and 4 mM Na2ATP adjusted to pH 7.3 with KOH) and 250 nL nystatin stock solution (100
260 mg/mL in DMSO) and filtered by 0.45 µm nanopore filter (Ultra free MC 0.45µm). Then a glass pipette
261 with the resistance of 7-10 MΩ was front-filled with 2 µL intracellular solution and then backfilled with
262 14 µL nystatin-containing intracellular solution. After quickly forming a GΩ seal with the target cell, we
263 waited until the access resistance became lower than 100 MΩ. Then, the membrane potential was
264 recorded in current-clamp mode with EPC10 Quadro amplifier (HEKA Electronik, Germany) using

265 PatchMaster software (HEKA Electronik, Germany) while simultaneously delivering a train of
266 holographic stimulation (6 μm circular pattern, 950 nm, 10 pulses of 20-ms duration delivered at 40 Hz)
267 and recording Ca^{2+} response with two-photon jRGECO1b imaging (1140 nm, 6.5 mW, 30 Hz). Imaging
268 power was set to ensure Ca^{2+} response was reliably detected. Only the cells that showed reliable firing in
269 response to the holographic stimulation were included in the analysis of imaging-induced depolarization.
270 The amount of depolarization by the imaging laser was quantified by calculating the difference in the
271 average membrane potential from the three-second window before the end of the imaging and that from
272 three-second window after the end of the imaging (10 trials).

273 Characterization of wavelength-dependent two-photon activation of CoChR

274 Current-clamp recording was performed from hindbrain neurons expressing CoChR-EGFP-Kv2.1 in
275 Tg[vsx2:Gal4; 10xUAS:CoChR-EGFP-Kv2.1] using the procedure described above but in a standard
276 whole-cell configuration. The patched cell was stimulated by scanning femtosecond laser with resonant-
277 galvo mirrors (6 μm x 6 μm, 2 ms duration) using two femtosecond laser sources to cover from 780 nm to
278 1220 nm in 40 nm steps (780- 980: MaiTai HP; 1020-1220: Insight HP). The power after the objective
279 lens was matched to 10 mW across wavelengths so that the none of the cells spiked an action potential
280 across all the wavelengths examined. The pulse width at each wavelength was measured with auto-
281 correlator (FEMTOCHROME Research, Inc., FR-103TPM/700). The resulting membrane depolarization
282 to the most effective wavelength for a given cell was averaged from at least 5 trials and then used to
283 normalize the response amplitude in individual trials. This normalized response was averaged over all the
284 trials pooled across cells. The resulting action spectrum is similar to published recordings[5], that here we
285 extend to a broader wavelength range.

286

287 ## Characterization of jRGECO1b in zebrafish sensory neurons

288 The sensitivity of jRGECO1b in zebrafish sensory neurons was examined as described previously[30].
289 Briefly, Tg[elavl3:Gal4;10xUAS:jRGECO1b] at 3 dpf were paralyzed by a 5-min bath application of 1
290 mg/ml a-bungarotoxin (Sigma, 203980). Larvae were mounted on their side in a field stimulation
291 chamber (Warner, RC-27NE2) with 1.5% low-melting-point agarose (Supplementary Fig. 2b). Tactile
292 sensory neurons (Rohon-Beard cells) were identified based on their oblong-shaped soma in the dorsal
293 spinal cord and their innervations to the skin using the two-photon microscope described above.
294 Functional images (256 × 256 pixels) were acquired at 7.5 Hz (1140 nm, 3 mW) while trains of 1, 2, 5,
295 10, and 20 field stimuli (1 ms pulse width at 50 Hz) were applied with a stimulator (NPI, ISO-STIM) to
296 stimulate the processes of the sensory neurons on the skin. This protocol elicits the corresponding number
297 of spikes in the sensory neurons[30]. The stimulation voltage was calibrated to elicit an identifiable response
298 to a single pulse in Rohon-Beard cells without stimulating muscle cells. Regions of interest were selected
299 manually, and data were analyzed using MATLAB (MathWorks). Two-photon absorption spectra of
300 jRGECO1b were collected by John Macklin as previously described[31] (Supplementary Fig. 2a).

301 ## Concurrent two-photon optogenetics and volumetric imaging

302 Tg[vsx2:Gal4;10xUAS:CoChR-EGFP-Kv2.1;10xUAS:jRGECO1b] at 5 dpf were used for this
303 experiment. The fish with high expression of CoChR-EGFP-Kv2.1 and jRGEOC1b were selected,
304 paralyzed with α-bungarotoxin (MilliporeSigma, 203980, MO), and then embedded in 1.6% low-melting
305 point agar. Each sample was left under the objective lens at least 40 minutes before starting the
306 experiment to minimize potential sample drifts during the experiment. A reference z-stack for jRGECO1b
307 was acquired (1140 nm, 512 x 512 x 100 slices, 0.76 x 0.76 x 2 μm). Then a single target cell was
308 selected for each stimulation session. A phase pattern for stimulating each target with a 6-μm diameter
309 disk pattern was calculated, taking into account the transformation matrix obtained in the calibration
310 described above. A train of ten 20 ms stimulation pulses was delivered at 10 Hz while monitoring Ca^{2+}

311 response by volumetric imaging of jRGEOC1b using the remote-focusing system (1140 nm, 512x256, 9
312 planes, 7 μm z step, 6 Hz, 6.5 mW) from 5 s before the stimulation to 14 s after the stimulation. To
313 identify neurons stimulated by this protocol during the experiments, we performed regression analysis as
314 described previously[26]. Briefly, two-photon data was first corrected for mismatch between the odd and
315 even scan lines by cross correlation and then the x-y movements were corrected for each slice by cross
316 correlation if necessary. A regressor for stimulation-induced activity was constructed by convolving the
317 stimulation pulses with a jRGECO1b impulse response function modeled as the rise and decay
318 exponentials (0.5 s rise and 2 s decay) and then standardized. The standardized coefficient was estimated
319 by ordinary least square and then *T* value for each pixel was calculated based on standardized coefficient
320 and residual. The activation map was used to determine the soma position of all the activated cells and
321 their distances to the intended targets were calculated using the transform from the remote-focusing
322 imaging space to the standard imaging space as described above. We repeated this procedure with
323 stimulation powers ranging from 1.2 mW to 12 mW to find the condition where only one cell is activated
324 for each stimulation target. ΔF/F0 was calculated by defining the baseline fluorescence (F0) as the
325 average fluorescence during the 4-s time window before the stimulation.

326 Synaptic connectivity mapping of spinal V2a neurons to spinal motoneurons

327 Whole-cell recordings from spinal primary motoneurons were performed from
328 Tg[vsx2:Gal4;10xUAS:CoChR-EGFP-Kv2.1;10xUAS:jRGECO1b] at 5 dpf using the procedure
329 described previously[26]. Briefly, the fish with high expression of CoChR-EGFP-Kv2.1 and jRGEOC1b
330 were selected, paralyzed with α-bungarotoxin, and pinned to a sylgard-coated dish with etched tungsten
331 pins. The spinal cord at muscle segment 23 was exposed by removing the muscles overlying the spinal
332 cord. A pipette was filled with the standard intracellular solution containing 0.01% of Alxea Fluor 647
333 hydrazide (Thermo Fisher Scientific) and a class of primary motoneurons, caudal primary motoneuron
334 (CaP), was targeted based on its large soma and proximity to the segmental boundary and the lateral

335 surface of the spinal cord. The stimulations of putative presynaptic spinal V2a neurons started 10 minutes
336 after forming a gigaohm seal so that the fluorescence of Alexa Fluor 647 does not leak to the red channel
337 used for jRGECO1b imaging. Single spinal V2a neurons were targeted by a 6 μm-diameter disk
338 illumination pattern. Ten 20-ms stimulation pulses were delivered at a 100-ms interval so that
339 postsynaptic potentials induced by each pulse can be separated temporally. Ca^{2+} responses of neighboring
340 V2a neurons were monitored by jRGECO1b imaging with the remote focusing system (512x256, 5
341 planes, 7 μm step, 10 Hz). The stimulation session was continued until the patched CaP neuron started to
342 depolarize more than 5 mV after establishing the whole-cell configuration. Then a series of z-stacks for
343 CoChR-EGFP-Kv2.1, jRGECO1b and Alexa Fluor 647 was acquired in the standard two-photon imaging
344 configuration from muscle segments 4 to 23.

345 The regression analysis was performed to detect all the cells activated by the stimulation using the
346 procedure mentioned above but with one modification. To isolate the stimulation induced Ca^{2+} response
347 from the Ca^{2+} response during spontaneous swimming, an additional regressor for spontaneous swimming
348 was constructed based on the slow subthreshold depolarization of PMNs observed during spontaneous
349 swimming[21]. Such depolarization was detected by a bandpass filter and then the regressor was constructed
350 by convolving a boxcar function representing the duration of swim with the jRGECO1b impulse response
351 function described above. The trials with more than one activated cell were excluded from further
352 analysis. Among the stimulation trials with only one activated cell, we detect postsynaptic potentials that
353 occurred within 20 ms from the onset of each stimulation pulse based on the spiking pattern we observed
354 in hindbrain neurons using the identical stimulation protocol. If such postsynaptic potentials occurred in
355 more than 5 stimulation pulses for a given activated cell and their rise times matched the rise times of
356 synaptic potentials[14], the cell was considered to have synaptic connection to the patched motoneuron (half
357 rise time = 0.57 ± 0.35 ms, n = 43). In some cases, slow depolarization with a much longer rise time was
358 observed consistently after the stimulation pulses (half rise time = 15.3 ± 5.4 ms, n = 74). Such slow
359 membrane depolarization eliciting input to primary motoneurons was previously characterized and

360 suggested to be caused by electrical coupling through neighboring motoneurons[14]. Thus, the cells that
361 produced such slow response in motoneurons were categorized as electrically coupled cells. To
362 reconstruct the position of each activated cell, a series of z-stacks was stitched with the stitching plugin
363 available through Fiji (https://fiji.sc/).The activated cell for each stimulation trial was identified in this
364 stitched z-stack based on the x-y position of the stage and the z position of the objective lens for each
365 trial, and further confirmed by manual inspection. In order to pool data from multiple fish, the positions of
366 the activated cells were transformed to a common space using a procedure similar to the one described
367 previously[21]. First, for a given rostrocaudal position, the midline was identified based on the presence of
368 central canal in Dodt gradient contrast image, and the dorsal edge and ventral edge of the spinal cord were
369 marked using segmented lines in Fiji. This procedure was repeated to define the dorsal and ventral edges
370 of the spinal cord from muscle segments 4 to 23. Then the distances from a given activated cell to the
371 nearest line segments for the dorsal and the ventral edge were calculated. Then the dorsoventral position
372 of a given activated cell was defined as $Distance_{ventral}/(Distance_{dorsal} + Distance_{ventral})$. To define the
373 rostro-caudal position within each segment, muscle segment boundaries were marked with single-segment
374 lines in Fiji. Then a line was extended from a given activated cell to the nearest segmental boundaries so
375 that the vector of this line is the vector sum of the nearest dorsal and ventral edges. Then the normalized
376 rostro-caudal position of a given activated cell within a segment was defined as
377 $Distance_{caudal}/(Distance_{rostral} + Distance_{caudal})$. The rostral caudal position of a given activated cell
378 relative to the patched CaP was defined as the sum of this normalized rostro-caudal position within a
379 segment and number of segments from the caudal end of the muscle segment where the recorded CaP was
380 located to the caudal end of the segment where a given activated cell was located. Then the two
381 dimensional distributions of synaptic connection probability, coupling probability and synaptic strength
382 were modeled with generalized additive models using the *mgcv* package (https://cran.r-
383 project.org/web/packages/mgcv/) in R (https://www.r-project.org/). This statistical technique is widely
384 used to model spatial data in ecology and epidemiology[32]. Probability distributions were modeled as a
385 combination of a full tensor product smooth (*te*) of the normalized dorsoventral position, a full tensor

386 product smooth (*te*) of the rostrocaudal position, and a tensor product interaction (*ti*) of the normalized
387 dorsoventral position and the rostrocaudal position with a logit link function for binomial distribution.
388 Synaptic strength was modeled similarly but with log transformed to satisfy the assumptions of the linear
389 model (normality, homogeneity of variance, independence and linearity). The tensor product interaction
390 was discarded to improve the concurvity of the model[32] (the worst case for the full model: 0.99; the worst
391 case for the model without the tensor product interaction: 0.38).

Acknowledgements

We thank A. Pujala and M. Tanimoto for critical feedback and helpful comments on the manuscript; J. Macklin and GENIE project for providing two-photon absorption spectra of jRGECO1b; V. de Sars for the development of the Wave Front Designer software for holographic phasemask calculation; V. Goncharov for help with our optical system. This work was supported by Howard Hughes Medical Institute, the National Institute of Health (Grant NIH 1UF1NS107574 - 01), the Fondation Bettencourt Schueller (Prix Coups d'élan pour la recherché française) and the Getty Lab.

399 # Author contributions

400 C.M. designed and built the remote-focusing system. D.T. designed and built the holographic stimulation
401 system. L.Z. generated Tg[10xUAS:CoChR-EGFP-Kv2.1], and managed the transgenic lines used in the
402 study. C.Y. and M.B.A. generated Tg[10xUAS:jRGECO1b]. M.K., C.M., and D.T. designed and
403 performed experiments, and interpreted data. M.K., D.T., and V.E. wrote the paper. M.K. and V.E.
404 conceived and supervised the project.

Competing interests

None.

407 # References

408 1. Petreanu, L., Huber, D., Sobczyk, A. & Svoboda, K. Channelrhodopsin-2–assisted circuit mapping of
409 long-range callosal projections. *Nat. Neurosci.* **10**, 663–668 (2007).
410 2. Chen, I.-W., Papagiakoumou, E. & Emiliani, V. Towards circuit optogenetics. *Curr. Opin.*
411 *Neurobiol.* **50**, 179–189 (2018).
412 3. Baker, C. A., Elyada, Y. M., Parra, A. & Bolton, M. M. Cellular resolution circuit mapping with
413 temporal-focused excitation of soma-targeted channelrhodopsin. *eLife* **5**, e14193 (2016).
414 4. Pégard, N. C. *et al.* Three-dimensional scanless holographic optogenetics with temporal focusing
415 (3D-SHOT). *Nat. Commun.* **8**, 1228 (2017).
416 5. Shemesh, O. A. *et al.* Temporally precise single-cell-resolution optogenetics. *Nat. Neurosci.* **20**,
417 1796–1806 (2017).
418 6. Klapoetke, N. C. *et al.* Independent optical excitation of distinct neural populations. *Nat. Methods* **11**,
419 338–346 (2014).
420 7. Chen, I.-W. *et al.* In Vivo Submillisecond Two-Photon Optogenetics with Temporally Focused
421 Patterned Light. *J. Neurosci.* **39**, 3484–3497 (2019).
422 8. Mu, Y. *et al.* Glia Accumulate Evidence that Actions Are Futile and Suppress Unsuccessful
423 Behavior. *Cell* **178**, 27-43.e19 (2019).
424 9. Ahrens, M. B., Orger, M. B., Robson, D. N., Li, J. M. & Keller, P. J. Whole-brain functional imaging
425 at cellular resolution using light-sheet microscopy. *Nat. Methods* **10**, 413–420 (2013).
426 10. Rupprecht, P., Prendergast, A., Wyart, C. & Friedrich, R. W. Remote z-scanning with a macroscopic
427 voice coil motor for fast 3D multiphoton laser scanning microscopy. *Biomed. Opt. Express* **7**, 1656–
428 1671 (2016).
429 11. Goulding, M. Circuits controlling vertebrate locomotion: moving in a new direction. *Nat Rev*
430 *Neurosci* **10**, 507–518 (2009).

431 12. Ampatzis, K., Song, J., Ausborn, J. & El Manira, A. Separate Microcircuit Modules of Distinct V2a
432 Interneurons and Motoneurons Control the Speed of Locomotion. *Neuron* **83**, 934–943 (2014).
433 13. Svara, F. N., Kornfeld, J., Denk, W. & Bollmann, J. H. Volume EM Reconstruction of Spinal Cord
434 Reveals Wiring Specificity in Speed-Related Motor Circuits. *Cell Rep.* **23**, 2942–2954 (2018).
435 14. Menelaou, E. & McLean, D. L. Hierarchical control of locomotion by distinct types of spinal V2a
436 interneurons in zebrafish. *Nat. Commun.* **10**, 1–12 (2019).
437 15. Fulton, B. P., Miledi, R. & Takahashi, T. Electrical synapses between motoneurons in the spinal cord
438 of the newborn rat. *Proc. R. Soc. Lond. B Biol. Sci.* **208**, 115–120 (1980).
439 16. Perrins, R. & Roberts, A. Cholinergic and electrical synapses between synergistic spinal
440 motoneurones in the Xenopus laevis embryo. *J. Physiol.* **485 (Pt 1)**, 135–144 (1995).
441 17. Kotaleski, J. H., Grillner, S. & Lansner, A. Neural mechanisms potentially contributing to the
442 intersegmental phase lag in lamprey. *Biol. Cybern.* **81**, 317–330 (1999).
443 18. Wolf, E., Soffe, S. R. & Roberts, A. Longitudinal neuronal organization and coordination in a simple
444 vertebrate: a continuous, semi-quantitative computer model of the central pattern generator for
445 swimming in young frog tadpoles. *J. Comput. Neurosci.* **27**, 291–308 (2009).
446 19. Hartenstein, V. Early pattern of neuronal differentiation in the Xenopus embryonic brainstem and
447 spinal cord. *J. Comp. Neurol.* **328**, 213–231 (1993).
448 20. Dale, N. Excitatory synaptic drive for swimming mediated by amino acid receptors in the lamprey. *J.*
449 *Neurosci.* **6**, 2662–2675 (1986).
450 21. McLean, D. L., Masino, M. A., Koh, I. Y. Y., Lindquist, W. B. & Fetcho, J. R. Continuous shifts in
451 the active set of spinal interneurons during changes in locomotor speed. *Nat. Neurosci.* **11**, 1419–
452 1429 (2008).
453 22. Kimura, Y. *et al.* Hindbrain V2a Neurons in the Excitation of Spinal Locomotor Circuits during
454 Zebrafish Swimming. *Curr. Biol.* **23**, 843–849 (2013).
455 23. Kimura, Y., Satou, C. & Higashijima, S. V2a and V2b neurons are generated by the final divisions of
456 pair-producing progenitors in the zebrafish spinal cord. *Development* **135**, 3001–3005 (2008).

457 24. Kwan, K. M. *et al.* The Tol2kit: A multisite gateway-based construction kit for Tol2 transposon
458 transgenesis constructs. *Dev. Dyn.* **236**, 3088–3099 (2007).
459 25. Abdelfattah, A. S. *et al.* Bright and photostable chemigenetic indicators for extended in vivo voltage
460 imaging. *Science* **365**, 699–704 (2019).
461 26. Pujala, A. & Koyama, M. Chronology-based architecture of descending circuits that underlie the
462 development of locomotor repertoire after birth. *eLife* **8**, e42135 (2019).
463 27. Hernandez, O. *et al.* Three-dimensional spatiotemporal focusing of holographic patterns. *Nat.*
464 *Commun.* **7**, 11928 (2016).
465 28. Gerchberg, R. W. & Saxton, W. O. A practical algorithm for the determination of phase from image
466 and diffraction plane pictures. *Optik* **35**, 237 (1972).
467 29. Lutz, C. *et al.* Holographic photolysis of caged neurotransmitters. *Nat. Methods* **5**, 821–827 (2008).
468 30. Higashijima, S., Masino, M. A., Mandel, G. & Fetcho, J. R. Imaging Neuronal Activity During
469 Zebrafish Behavior With a Genetically Encoded Calcium Indicator. *J. Neurophysiol.* **90**, 3986–3997
470 (2003).
471 31. Dana, H. *et al.* Sensitive red protein calcium indicators for imaging neural activity. *eLife* **5**, e12727
472 (2016).
473 32. Wood, S. N. *Generalized Additive Models: An Introduction with R, Second Edition*. (Chapman and
474 Hall/CRC, 2017).
475